JGR Atmospheres

RESEARCH ARTICLE
10.1029/2026JD046394

Impacts of Urbanization on Atmospheric Oxygen: High-Resolution Observational Evidence

Li Wang[1], Jianping Huang[1], Changyu Li[1], Kaihui Zhao[2], Jinsen Shi[3], and Dongliang Han[1]

[1]Collaborative Innovation Center for Western Ecological Safety, Lanzhou University, Lanzhou, China, [2]Yunnan Key Laboratory of Meteorological Disasters and Climate Resources in the Greater Mekong Subregion, Yunnan University, Kunming, China, [3]Key Laboratory for Semi-Arid Climate Change of the Ministry of Education, College of Atmospheric Sciences, Lanzhou University, Lanzhou, China

Key Points:

- High precision observations reveal distinct controls on O_2 variability at remote and urban sites
- Remote O_2 variability is governed mainly by meteorology, whereas urban O_2 depletion reflects meteorology-emission coupling
- Urban O_2 depletion shifts from physical decoupling in aerosol pollution to chemical synergy in ozone pollution

Supporting Information:

Supporting Information may be found in the online version of this article.

Correspondence to:

J. Huang,
hjp@lzu.edu.cn

Citation:

Wang, L., Huang, J., Li, C., Zhao, K., Shi, J., & Han, D. (2026). Impacts of urbanization on atmospheric oxygen: High-resolution observational evidence. *Journal of Geophysical Research: Atmospheres*, *131*, e2026JD046394. https://doi.org/10.1029/2026JD046394

Received 13 JAN 2026
Accepted 15 APR 2026

Author Contributions:

Conceptualization: Li Wang, Jianping Huang
Data curation: Li Wang, Changyu Li, Kaihui Zhao, Jinsen Shi, Dongliang Han
Funding acquisition: Li Wang, Jianping Huang
Investigation: Changyu Li, Kaihui Zhao, Jinsen Shi, Dongliang Han
Methodology: Li Wang
Resources: Jianping Huang, Changyu Li, Kaihui Zhao, Jinsen Shi, Dongliang Han
Supervision: Jianping Huang
Visualization: Li Wang
Writing – original draft: Li Wang
Writing – review & editing: Li Wang, Jianping Huang

Abstract Oxygen (O_2), a fundamental constituent of Earth's atmosphere, sustains aerobic life and maintains the equilibrium of global biogeochemical cycles. However, rapid urbanization is increasingly perturbing the natural O_2 balance, yet the distinct mechanisms driving these perturbations remain poorly understood. Here, we report the first simultaneous, high-precision in situ O_2 observations at two contrasting sites: an industrial urban valley (Lanzhou) and a remote high-altitude background site (Qomolangma Station). By disentangling meteorological confounders, we reveal a fundamental divergence in the controls on atmospheric O_2 variability: the remote baseline is primarily controlled by meteorological variability, especially temperature-pressure coupling, whereas urban O_2 variability in the valley reflects the interaction between local anthropogenic emissions and large-scale weather patterns that regulate atmospheric stability and dispersion. Crucially, mechanistic analyses of urban atmospheric oxygen depletion reveal a regime-dependent transition in its dominant controls: (a) Aerosol pollution is marked by "physical decoupling", where external transport disrupts the linearity between local combustion and oxygen deficits; (b) Ozone pollution, conversely, exhibits "chemical synergy", driven by temperature-enhanced precursor oxidation and associated secondary transformations. These findings establish urban O_2 variability as an integrator of anthropogenic emissions and atmospheric oxidation capacity, underscoring the necessity of incorporating chemical-meteorological feedbacks into assessments of urban ecosystem sustainability and carbon budgets.

Plain Language Summary Oxygen is essential for life, but rapid urbanization is altering its natural balance in the atmosphere. Through the first simultaneous high-precision observations at an industrial urban valley (Lanzhou) and a remote background site (Qomolangma Station), We discovered that unlike remote areas driven by simple natural cycles, urban oxygen levels are governed by a complex mechanism that shifts between being dominated by physical transport and active chemical transformations, depending on the specific pollution environment. These findings demonstrate that urban oxygen depletion is not just a result of fossil fuel combustion but is actively modulated by the complex interaction between weather dynamics and atmospheric chemistry.

1. Introduction

Oxygen (O_2) is the most abundant element on Earth and participates in numerous chemical reactions, including biogeochemical cycles of fundamental elements such as carbon, sulfur, nitrogen, and phosphorus. For example, photosynthesis continuously releases O_2 into the atmosphere, whereas biological respiration and organic matter combustion consume O_2, forming a coupled and inverse cycle with atmospheric carbon dioxide (Huang et al., 2021). These biogeochemical cycles sustain life on Earth and play a crucial role in climate regulation, thereby possessing significant climatic, economic, and societal relevance. Increasing evidence suggests that human activities, particularly the combustion of fossil fuels, can profoundly disrupt these biogeochemical cycles. One of the most prominent features recorded is a measurable decline in atmospheric O_2 concentrations. This decrease is primarily driven by anthropogenic fossil fuel emissions, with partial compensation from land and ocean outgassing (Keeling & Manning, 2014). As cities have the highest population densities and most intensive fossil fuel use, they represent major hotspots for atmospheric O_2 consumption. Therefore, it is of great importance to conduct real-time observation and analysis of atmospheric O_2 concentration.

Measurements of atmospheric O_2 provide unique insights into biogeochemical cycles beyond those attainable from carbon and its isotopes alone (Bender et al., 1998; Keeling et al., 1993). However, the high ambient

concentration of O_2 (20.95%) makes it technically challenging to detect subtle changes. Consequently, a range of high-precision techniques have been developed to meet these demands, including optical interferometry (Keeling et al., 1993), paramagnetic oxygen analyzers (Manning et al., 1999), mass spectrometry (Bender et al., 1998), gas chromatography (Tohjima, 2000), vacuum ultraviolet absorption and fuel cell methods (Morgan et al., 2019), as well as the emerging cavity ring-down spectroscopy (Fleming et al., 2023). The Keeling team established the first atmospheric O_2 monitoring network, which remains the longest-running record of its kind (https://scrippso2.ucsd.edu/). Since then, research groups worldwide have increasingly focused on atmospheric O_2, expanding ground-based observations from global background sites to regional and urban stations.

Observational and modeling studies related to atmospheric O_2 span distinct timescales, ranging from multi-decadal trends to seasonal and diurnal fluctuations. From a multidecadal perspective, there has been a gradual but continuous decline in global atmospheric O_2 levels over recent decades. Since the late 1980s, atmospheric O_2 has declined steadily at ∼4 ppm/yr (Keeling & Manning, 2014). This long-term trend is driven primarily by anthropogenic O_2 consumption, especially that associated with large-scale fossil fuel combustion (Huang et al., 2021). According to Huang et al. (2018), under the RCP8.5 scenario, the enhancement of photosynthetic O_2 production is insufficient to offset the rapid rise in anthropogenic O_2 consumption, resulting in a progressively widening imbalance between O_2 production and consumption. By the end of the 21st century, this imbalance is projected to remove approximately 100Gt of O_2 from the atmosphere each year. This rate corresponds to about 0.008% of the total atmospheric O_2 reservoir per year, given an atmospheric O_2 inventory of the order of 1.2×10^6Gt. At regional and urban scales, this imbalance may become even more pronounced because of concentrated anthropogenic activities. In addition to fossil fuel combustion and human respiration, deforestation and land-use change may further weaken the capacity of terrestrial ecosystems to replenish atmospheric O_2. Wei et al. (2021) assessed O_2 imbalances in cities with populations exceeding 1 million, demonstrating that O_2 consumption significantly surpasses local O_2 production. High-frequency observations at local and city scales further demonstrate that atmospheric O_2 exhibits pronounced periodicity and spatiotemporal variability driven by the combined effects of anthropogenic emissions and meteorological mixing. Liu et al. (2023) revealed that urban O_2 dynamics are shaped by distinct temporal drivers. Diurnally, traffic-related fossil fuel combustion causes notable minima during rush hours. Seasonally, O_2 levels are highest in summer due to vegetation photosynthesis and strong atmospheric mixing, while dropping to their lowest in winter. This winter depletion is driven by the synergistic effects of increased domestic heating, diminished photosynthetic activity, and unfavorable meteorological conditions, such as surface inversions that trap pollutants and limit dispersion. By contrast, in remote natural regions with limited anthropogenic influence, O_2 variability is governed mainly by natural factors such as altitude, near-surface air temperature, and vegetation dynamics (Hu et al., 2023; Shi et al., 2021). Taken together, these findings highlight atmospheric O_2 as a sensitive tracer of anthropogenic activity and atmospheric transport, with important applications in studies of local-to-regional environmental change. Atmospheric O_2 measurements also provide important constraints on carbon-cycle processes (Keeling et al., 1996; Manning & Keeling, 2006) and on the independent quantification of fossil fuel emissions (Pickers et al., 2022).

Nevertheless, existing studies primarily focus on global O_2 trends or total O_2 budgets, resulting in an inadequate understanding of the mechanisms driving localized atmospheric O_2 fluctuations. Limited long-term data on urban O_2 concentrations further restrict our ability to quantify how anthropogenic activities alter local oxidation ratios. Moreover, few studies have integrated the synergistic influences of multiple drivers, obscuring the regional heterogeneities and specific disruptions to the oxygen cycle arising from the interplay between emissions and climate variability. To address these gaps, this study systematically investigates atmospheric O_2 variability using high temporal resolution observations at two contrasting sites: an industrial urban station in Lanzhou and a remote high-altitude plateau station on Mount Qomolangma. The primary objective is to decouple the complex interplay between meteorological modulations and anthropogenic drivers that govern O_2 dynamics across these distinct environments. Furthermore, we examine the mechanistic response of the urban oxygen cycle under varying atmospheric pollution scenarios to better understand the coupling between local emissions and air quality dynamics. By integrating multisource data sets and accounting for meteorological confounders, this research evaluates the utility of atmospheric O_2 as a sensitive integrator of regional carbon-oxygen dynamics, thereby offering key insights to better constrain chemical-meteorological feedbacks within urban carbon cycle and sustainability assessments.

2. Materials and Methods

2.1. Site Locations

High-precision urban atmospheric O_2 concentration measurements were obtained from the Lanzhou University in situ atmospheric O_2 observation platform (Liu et al., 2023), hereafter referred to as the "Lanzhou station", located in the northwest industrial hub of Lanzhou (elevation 1,520 m), which lies within a semi-enclosed, dumbbell-shaped river valley surrounded by mountain ranges. Since July 2020, the platform has performed continuous online measurements of ambient O_2. To provide a concurrent comparison for inter-regional analysis, continuous atmospheric O_2 monitoring was also carried out at the Qomolangma Station of the China Academy of Sciences (QOMS: elevation 4,276 m, Sun et al., 2018) from August to October 2024, under the framework of the Second Tibetan Plateau Scientific Expedition and Research (STEP) program. During this period, parallel measurements were conducted at both sites (Figure S1 in Supporting Information S1) using identical Picarro G2207-i gas concentration and isotope analyzers (Collaborative Innovation Center for West Ecological Safety, 2025). As illustrated in Figure S2 of Supporting Information S1, land use and land cover (LULC) within a 5 km radius of each site were analyzed using the Esri 10-m resolution data set. The Lanzhou Station is predominantly characterized by "Built Area", followed by "Rangeland" and "Water." Because its urban river valley setting restricts atmospheric dispersion, the station exhibits strong sensitivity to near-field anthropogenic emissions. It is noted that the "Rangeland" class in this data set identifies the spectral features of semi-arid vegetation (grass and shrubs). In contrast, the Qomolangma Station is located in a remote high-altitude environment and serves as a background site. The surrounding landscape is dominated by natural "Rangeland" and "Bare Ground" with negligible anthropogenic land use. Driven by its elevated altitude and lack of local emission sources, the station is representative of a broader background footprint extending well beyond the immediate local surroundings, making it ideal for monitoring regional baseline conditions.

2.2. Measurements for Atmospheric O_2

The Picarro G2207-i gas concentration and isotope analyzers utilize cavity ring-down spectroscopy (CRDS), achieving an effective optical path length of up to 20 km within a compact cavity. This enables tabletop instruments to deliver exceptional precision and sensitivity. In this study, the two Picarro G2207-i analyzers achieved O_2 mole fraction precisions of 1.7 and 1.99 ppm, respectively, defined as the 1σ standard deviation of 5-min averaged data over a 4-hr period. Their corresponding 24-hr drifts were 3 and 2 ppm, respectively, calculated as the difference between the maximum and minimum of the 60-min averaged raw data over 24hr. The design and operating principles of this analyzer were described in detail by Fleming et al. (2023). Although CRDS instruments apply internal water-vapor corrections to achieve ppm-level accuracy in dry-air O_2 measurements, we installed a front-end dehumidification system using an upstream Nafion dryer to further reduce water-vapor interference.

The Picarro G2207-i simultaneously measures O_2 and H_2O and applies an undocumented internal water-vapor correction to report a water-corrected dry-air O_2 mole fraction (O_2, WC). The raw channel (O_2, NC) is affected by dilution from water vapor as well as spectroscopic effects. In the early phase of this study, we conducted comparative experiments to evaluate the performance of the instrument's internal water-vapor correction with and without the additional front-end dehumidification system. As shown in Figure S3 of Supporting Information S1, in the absence of the external dehumidification system (Figures S3a and S3b in Supporting Information S1), wet O_2 (O_2, NC) exhibits a very strong correlation with water vapor (H_2O) ($R^2 = 0.998$), indicating a pronounced dilution effect of water vapor on the O_2 measurements, after the internal water-vapor correction is applied, dry O_2 (O_2, WC) still shows a residual correlation with water vapor ($R^2 = 0.174$), suggesting that the internal correction alone cannot fully remove water-vapor interference, particularly under high-humidity conditions. When the external dehumidification system is activated (Figures S3c and S3d in Supporting Information S1), the dependence of the O_2 measurements on water vapor is substantially reduced. For wet O_2 (O_2, NC), the correlation between water vapor and O_2 is greatly weakened ($R^2 = 0.054$), and for dry O_2 (O_2, WC), the correlation is nearly negligible ($R^2 = 0.001$). Furthermore, comparative measurements of ambient O_2 at an outdoor station show that (Figure S4 in Supporting Information S1 and Figure 5), under identical water-removal conditions, the two Picarro instruments agree closely ($R^2 = 0.993$), indicating negligible systematic bias. Overall, these results demonstrate that the external water-vapor removal system effectively reduces water-vapor interference and improves the accuracy of O_2 measurements.

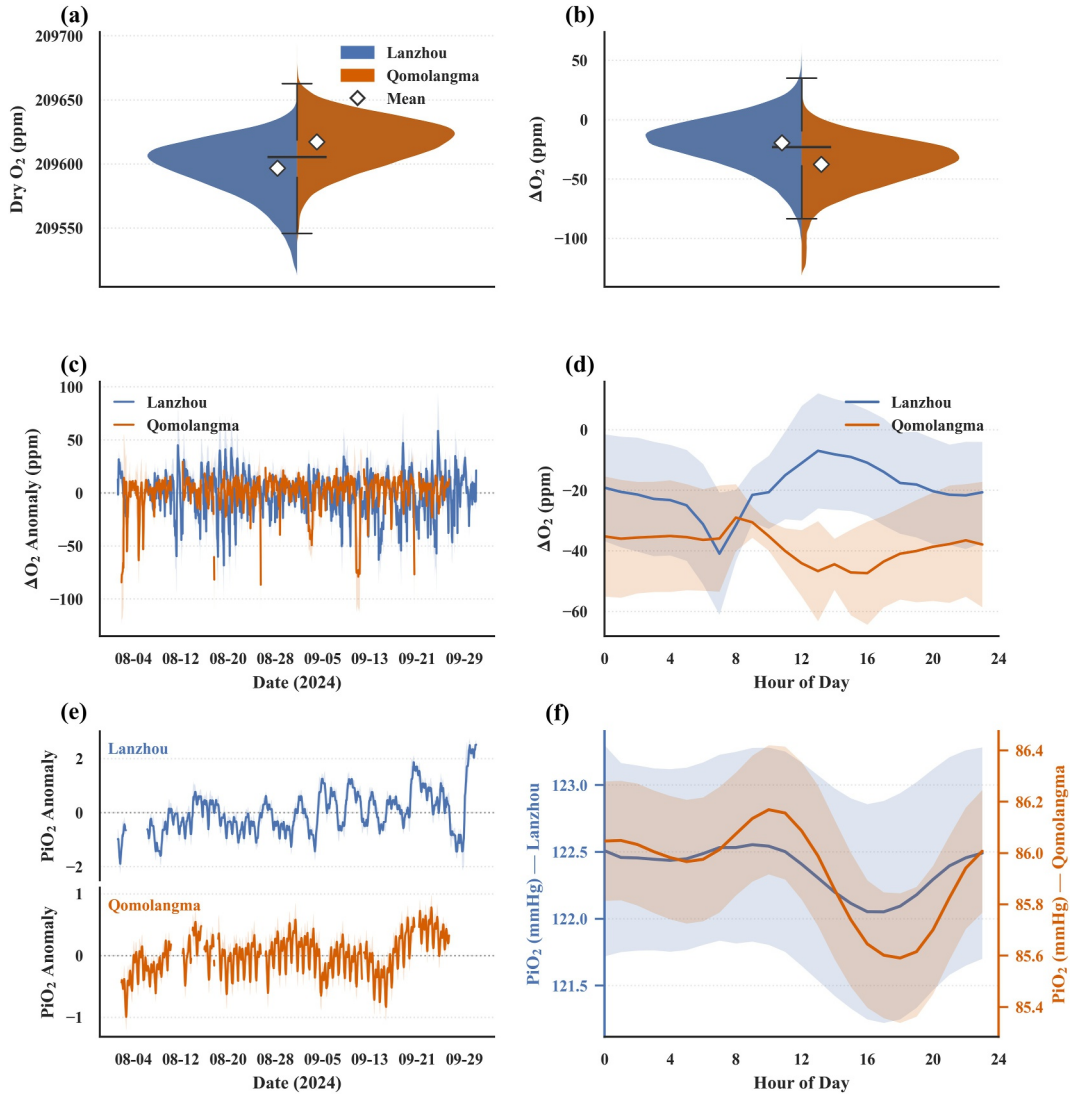

Figure 1. Split-violin plots of (a) dry atmospheric O_2 and (b) ΔO_2 for August–September 2024 at Lanzhou (blue) and Qomolangma (orange). Each half-violin shows the kernel density distributions; embedded boxplots indicate the interquartile range (whiskers = 1.5 × IQR), with diamonds and circles denoting the mean and median, respectively. Panel (c) shows hourly ΔO_2 anomalies (deviations from each station's August–September mean), and panel (e) the corresponding inspired PiO_2. In (c, e), shaded bands represent ± 1 standard deviation from a 24-hr running mean of the hourly values (short-term variability), whereas in (d, f) they represent ± 1 standard deviation across all days for each hour of the day (day-to-day variability).

2.3. Data Quality Control

Atmospheric O_2 was measured with two Picarro G2207-i analyzers, and the same standard gas mixture was used at both Lanzhou and the Qomolangma stations, thereby eliminating inter-station calibration offsets. During each calibration, both analyzers were connected to a certified reference gas, the standard was introduced to the instrument inlet and, once the readings stabilized, the mean value over the selected interval was taken. For comparison, Fleming et al. (2023) measured each cylinder for 20 min with the first 8 min discarded as equilibration. In our study, each cylinder was measured for 30 min, with the first 12 min treated as equilibration. The standard gas was a synthetic-air certified reference material (CRM) from the National Institute of Metrology (NIM), China, with 21.01% O_2 (balance N_2) in a high-pressure steel cylinder. During the entire observation period, the cylinder was stored indoors at room temperature, and the valve remained closed except during calibration to avoid unnecessary gas loss. As shown in Figure S6a of Supporting Information S1, during the selected stable periods, the

O_2 concentrations measured by both instruments were highly stable, with standard deviations of 1.28 ppm for Picarro1 and 1.35 ppm for Picarro2. The fitted lines were nearly horizontal, indicating negligible short-term drift within an individual calibration run. In contrast, both instruments exhibited a similar long-term change in the mean standard-gas response over the approximately 1-year interval, at about −0.24% relative to the 21.01% reference (Figure S6b in Supporting Information S1), indicating consistent instrument behavior and suggesting no leakage or degradation of the calibration cylinder.

The Picarro analyzers recorded dry O_2 mole fractions at a native 1s resolution. To reduce high-frequency noise and facilitate inter-site alignment, the 1s data were first averaged to 5s. Periods affected by instrument warm-up, power interruptions, maintenance, or abnormal diagnostic flags were removed. Statistical outliers in dry O_2 were then filtered using a median absolute deviation (MAD) method to eliminate spike-like anomalies in ΔO_2. Intervals with clusters of outliers and periods around maintenance or known local contamination events were additionally checked visually to avoid removing genuine atmospheric variability. After all QC steps, 96.5% of the 5 s O_2 data at Lanzhou and 90.5% at Mount Qomolangma were retained, indicating that only a small portion of the original observations was removed and that the diurnal statistics are based on well-sampled data.

To isolate temporal variability from inter-site baseline differences caused by altitude-related background gradients and residual calibration offsets, we expressed O_2 as site-specific anomalies, $\Delta O_{2\_i(t)}$, where i denotes site and t denotes hour time step. For each site i and each hour t, we defined a dynamic baseline $O_{2\_baseline,i(t)}$, as the 99th percentile of the calibrated dry O_2 mole fractions within a 24 hr window centered on t. This percentile time series was then smoothed with a 24 hr running mean to remove sub-daily variability. The hourly O_2 anomaly was calculated as

$$\Delta O_{2\_i(t)} = O_{2\_i(t)} - O_{2\_baseline,i(t)} \quad (1)$$

where $O_{2\_i(t)}$ is the calibrated dry O_2 mole fraction measured at site i and hour t. $O_{2\_baseline,i(t)}$ is the corresponding site-specific dynamic baseline. This high-percentile, moving-window approach to derive a dynamic baseline is consistent with previous O_2/N_2 studies (Liu et al., 2023; Pickers et al., 2022).

To assess the sensitivity of our results to baseline definition, we constructed an alternative baseline for the Lanzhou urban site using nighttime observations (22:00–06:00) from candidate clean-air sectors under stable meteorological conditions. A continuous baseline was then derived using a rolling median followed by smoothing. The resulting ΔO_2 series (Figure S7 in Supporting Information S1) was highly consistent with that derived from the main percentile-based method ($R = 0.946$; bias = +2.169 ppm), indicating that the principal conclusions are not strongly sensitive to the baseline definition.

2.4. Measurements for Atmospheric Pollutants and Meteorological Parameters

The pollutant and meteorological observation data used to elucidate the mechanisms behind atmospheric O_2 variation are all sourced from online monitoring instruments at the respective stations (Urban Climate and Environment Observatory of Lanzhou University, 2022). Specifically, particulate matter (PM_{10}, $PM_{2.5}$, PM_1, and TSP; μg m^{-3}) is monitored with a 5030i SHARP PM synchronized hybrid analyzer. Trace gases are quantified using a suite of Thermo Fisher Scientific online analyzers—models 49i, 42i, 48i, and 43i-for NO_x, NO, NO_2, SO_2, and O_3 (μg m^{-3}) and for CO (mg m^{-3}). Particulate carbon species, including organic carbon (OC), elemental carbon (EC), and total carbon (TC), were measured using a Sunset Laboratory online carbon aerosol analyzer. Black carbon (BC) concentrations were determined by an AE33 analyzer. Meteorological parameters: air temperature (°C), relative humidity (RH, %), wind speed (WS, m s^{-1}), and wind direction (WD) were recorded using an FWS500 meteorological sensor. Vertical meteorological profiles were obtained using an MWP967KV analyzer. Downwelling solar radiation (W m^{-2}) is recorded with a Kipp & Zonen SMP22 pyranometer, and visibility (km) is determined by a DNQ-2 visibility sensor. Vertical profiles of temperature and humidity were derived from continuous microwave radiometer observations. In the integrated analysis, the ΔO_2 anomalies (defined in Section 2.3) were directly integrated with pollutant concentrations, as their numerical magnitudes are comparable. Meteorological and environmental variables were utilized in their original physical units as the tree-based gradient boosting model (XGBoost) employed in this study is inherently invariant to feature scaling. All data processing, statistical analyses, and visualization workflows were performed in Python within JupyterLab, using open-source scientific libraries (Anaconda, Inc., 2023).

2.5. XGBoost Model and Trajectory Analysis

Gradient tree boosting algorithm (XGBoost) was employed to model ΔO_2, using CART regression trees as base learners. The analysis used high temporal resolution atmospheric O_2 measurements from Aug to Sep 2024 campaigns at Lanzhou and Qomolangma stations. Input features included co-located in situ surface meteorology (air temperature, relative humidity, surface pressure, wind speed and direction) and ERA5 reanalysis fields, both time-matched to the O_2 observations. To capture the continuous and cyclical nature of temporal variations, we applied trigonometric encoding to the timestamps derived from the raw data sets. Specifically, the Hour of Day and Day of Year were transformed into sine and cosine components (collectively referred to as the "Trend/Seasonality" feature group). This encoding strategy eliminates numerical discontinuities at temporal boundaries and ensures that the model correctly captures the recurring diurnal and seasonal phases. All timestamps were converted to Beijing Time. Model training used second-order (Taylor) loss approximation with L1 and L2 regularization to jointly control prediction error and model complexity. Data were split 70/30 into training and test sets. Performance was evaluated using R^2 and mean squared error (MSE). To enhance interpretability, we used tree-based SHAP (Shapley Additive Explanations) to quantify sample-level feature contributions and global importance (Padarian et al., 2020). Computational details are provided in the Text S1 of Supporting Information S1. SHAP values represent each feature's marginal contribution relative to the global mean prediction: positive values indicate a positive effect on ΔO_2, negative values indicate a negative effect, and larger absolute magnitudes denote stronger effects.

Back trajectories were calculated using the Hybrid Single-Particle Lagrangian Integrated Trajectory model (HYSPLIT) via the PySPLIT interface. Trajectories were initialized at 500, 1,000, and 1,500 m AGL (above ground level) over Lanzhou and integrated backward for 72 hr. GDAS1 meteorological fields (Global Data Assimilation System; 1° × 1°, 3-hourly) were used to drive the trajectory calculations. Hourly trajectory endpoints were then clipped to the study region for subsequent analysis. Vertical motion followed the default HYSPLIT model vertical velocity option. Over the study period, 150 back trajectories were generated for aerosol-pollution episodes and 240 for ozone-pollution episodes. In post-processing, trajectories were resampled at equal time steps to a fixed length via linear interpolation in longitude and latitude, and the resulting feature vectors were clustered with K-means to identify dominant transport pathways. For each cluster, an average (representative) trajectory and the mean path length were derived. Cluster-mean ΔO_2 was obtained by matching cluster assignments by date to surface ΔO_2 observations, and between-cluster differences were assessed with one-way ANOVA where per-cluster sample sizes allowed.

3. Results and Discussion

3.1. Atmospheric Oxygen Trends at Lanzhou and Qomolangma Stations

Atmospheric O_2 status can be characterized by two principal indicators: the relative change in atmospheric O_2 content (ΔO_2) and the inspired partial pressure of oxygen (PiO_2). The hourly ΔO_2 anomalies (in ppm) recorded at the Lanzhou and Qomolangma stations from August to September 2024 cluster around 209,600 ppm at both sites (Figure 1a). The Qomolangma station exhibits a distribution skewed toward negative values with a lower mean compared to Lanzhou. The Lanzhou data is clustered more symmetrically. The standard deviation of ΔO_2 at Lanzhou (18.73 ppm, calculated from hourly averages) exceeds that at the Qomolangma station (16.40 ppm) (Figure 1b). Given that this observed variability is nearly an order of magnitude larger than the instrument precision (~1.7–2.0 ppm), the spread reflects real atmospheric O_2 fluctuations rather than measurement noise. The greater variability at Lanzhou (Figure 1c) is likely a result of intensified anthropogenic activities, which manifest as periodic patterns in the time series (Ginzburg et al., 2023). At Lanzhou, ΔO_2 displays bimodal oscillations with ≈24 and 12 hr periodicities, peaking around 10:00–12:00 and 16:00–18:00, coinciding with morning and afternoon traffic rush hours and industrial activity. In contrast, the Qomolangma station shows a much smoother curve without a distinct bimodal pattern. Furthermore, PiO_2 at Lanzhou is substantially higher than that at the Qomolangma station (Figure 1e). Frequency-domain analysis based on power spectral density (Figure S8 in Supporting Information S1) further confirms that O_2 concentration fluctuations at Lanzhou are significantly greater than at Qomolangma station across both low-frequency (0.01–0.1 Hz, corresponding to periods of 10–100 hr) and high-frequency (0.1–1 Hz, periods of 1–10 hr) bands, with all differences statistically significant ($p < 0.05$).

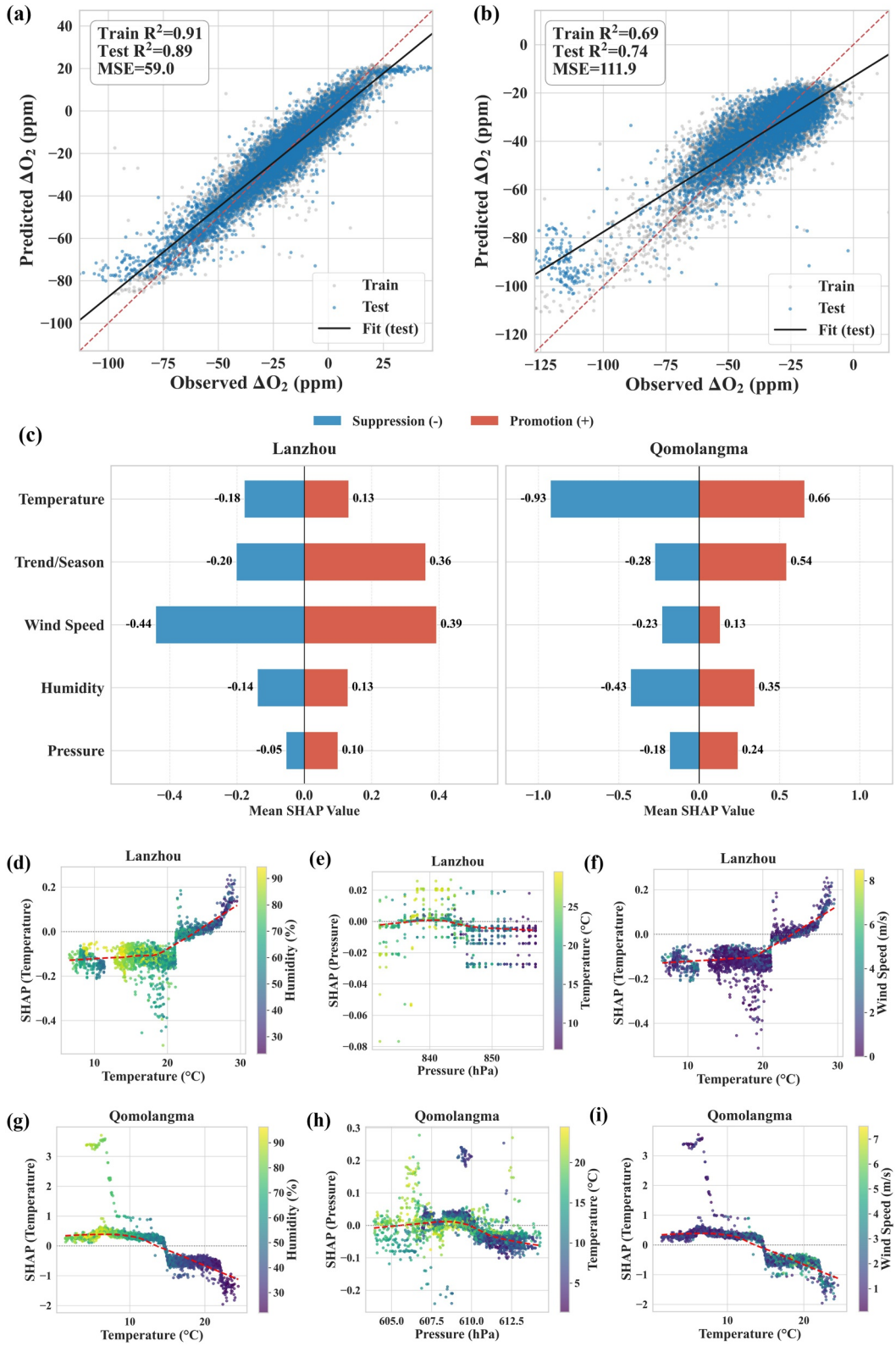

Figure 2. ΔO_2 model performance and SHAP interpretation at Lanzhou (a, c, d, e, f) and Qomolangma station (b, c, g, h, i): (a, b) Predicted versus observed ΔO_2 scatter plots with R^2 and MSE; (c) Diverging bar chart of aggregated feature impacts; red and blue bars denote positive (promoting) and negative (suppressing) contributions, respectively. Panels (d–i) SHAP dependence plots for Temperature, Humidity, Wind Speed, and Pressure. The dashed red line represents the LOWESS trend, highlighting the average non-linear physical response by filtering out random noise.

Figures 1d and 1f illustrate the 24-hr profiles of ΔO_2 and PiO_2, respectively. To ensure a meaningful comparison of diurnal variations between the two sites, which are located at different longitudes, all time series data were converted from Beijing Time to local solar time. The diurnal patterns at the two sites reflect the distinct coupling between local meteorological conditions and anthropogenic activities. At Lanzhou, ΔO_2 displays a pronounced diurnal cycle consistent with the diurnal rectifier effect, reflecting the covariance between near-surface sources/sinks and the diurnal evolution of boundary layer mixing (Denning et al., 1996; Larson & Volkmer, 2008). Specifically, ΔO_2 reaches a minimum in the early morning (around 07:00), when combustion-related signals accumulate within a shallow and stable nocturnal boundary layer, and increases toward an early afternoon maximum (~13:00) as boundary layer growth and enhanced vertical mixing dilute the near-surface signal, possibly with an additional contribution from daytime photosynthetic O_2 release (Liu et al., 2023). In contrast, ΔO_2 at the Qomolangma station remains relatively stable throughout the day, consistent with a representative background atmosphere with minimal local surface sources or sinks and a dominant influence of regional atmospheric transport. Similarly, PiO_2 at Lanzhou rises from approximately 122.1 mm Hg in the early morning to a maximum of about 122.6 mm Hg near midday and then declines after sunset. At the Qomolangma station, PiO_2 increases from about 85.6 mm Hg before dawn to a peak of 86.2 mm Hg close to local noon, and gradually decreases to around 85.9 mm Hg by late evening. Although the absolute diurnal variation in PiO_2 at both sites is less than 1 mm Hg, the relative change is greater at high altitude (~0.7%) than at low altitude (~0.4%). This suggests that at high elevations, the influence of meteorological pressure fluctuations on available oxygen (PiO_2) is relatively more pronounced than in low-altitude urban environments.

3.2. Meteorological Drivers of Atmospheric Oxygen Variability

Figures 2a and 2b demonstrate the robust fitting performance of the XGBoost models. The urban Lanzhou station exhibited high accuracy (Test $R^2 = 0.89$) with minimal training-testing disparity (Gap ≈ 0.02), reflecting the effective capture of regular urban signals. Despite higher noise levels at the high-altitude Qomolangma station, the model maintained comparable robustness. Notably, the fitted slopes in both figures fall slightly below the 1:1 line. This variance compression is not a defect but a result of the model's regularization mechanisms, which deliberately suppress prediction amplitude to prevent overfitting to random noise and ensure generalization (Hoerl & Kennard, 1970). By prioritizing global trends over point-to-point matching of extreme values, the model achieves a strictly constrained estimation.

Residual analysis was conducted to screen for systematic physical bias. The distribution of residuals (Observed—Predicted) for both stations exhibits a highly symmetric Gaussian shape centered strictly at zero (Figure S9 in Supporting Information S1), indicating that the models are globally unbiased and devoid of systematic mean deviation (Willmott, 1981). Furthermore, LOWESS (Locally Weighted Scatterplot Smoothing) trend lines (Figures S10a–S10f in Supporting Information S1) reveal that the residuals generally adhere to a horizontal zero line (Cleveland, 1979). For Lanzhou, slight non-linear deviations occur only under extreme conditions (e.g., high wind speeds), reflecting the complexity of transient anthropogenic disturbances. In contrast, Qomolangma exhibits remarkably flat trends across all intervals. This suggests that the ΔO_2 dynamics are dominated by large-scale thermal circulation, allowing the model to successfully isolate dominant driving mechanisms and leaving residuals as uncorrelated white noise.

SHAP analysis (Figure 2c) revealed distinct driving mechanisms for the two sites. Lanzhou is characterized by a wind speed-dominated dispersion mechanism (Mean SHAP ≈ 0.40). The balanced positive and negative contributions reflect wind's dual role: scavenging oxygen-depleted air versus dispersing photosynthetically enriched air. Conversely, Qomolangma exhibits a temperature-dominated thermal mechanism, where temperature exerts a strong negative suppression on ΔO_2. The prominence of the "Trend/Season" feature suggests that oxygen variations here are governed by natural diurnal and seasonal rhythms rather than anthropogenic interference. Figures 2d–2i illustrate the interactive effects. In Lanzhou, warming generally promotes ΔO_2, a positive contribution amplified by high humidity and wind speed, while atmospheric pressure has negligible impact. Qomolangma, however, displays significant thermal non-linearity. Below 10°C, cool and humid conditions boost ΔO_2; above 12°C, the trend sharply reverses, with warm, dry, and windy conditions exerting a dampening effect. Notably, high pressure (>610 hPa) coupled with low temperatures exerts a strong negative impact. This corresponds to static stability under high-pressure control, which suppresses atmospheric exchange and hinders the replenishment of local oxygen levels.

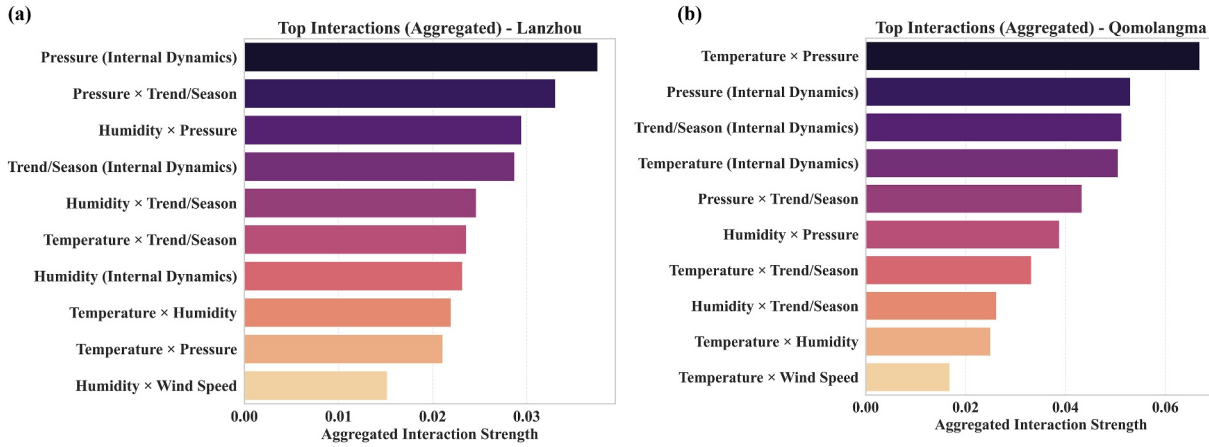

Figure 3. Ranking of dominant feature interactions based on aggregated SHAP values. Top interacting feature pairs for (a) Lanzhou and (b) Qomolangma.

Figure 3 elucidates the detailed non-linear coupling mechanisms. In Lanzhou, the dominant term is "Pressure (Internal Dynamics)." This metric, aggregating SHAP interaction strengths across multi-source and multi-scale pressure features (e.g., instantaneous, rolling means, ERA5), reveals that ΔO_2 non-linearity is largely driven by the co-evolution of internal pressure variables. Secondary drivers like "Pressure × Trend/Season" and "Humidity × Pressure" further highlight the critical role of pressure coupling with temporal phases and humidity. In contrast, Qomolangma is dominated by "Temperature × Pressure", indicating a high sensitivity to the joint variation of thermal and dynamic factors. This is followed by the internal dynamics of "Pressure" and "Trend/Season", emphasizing the prominence of diurnal and seasonal rhythms in regulating local oxygen levels. Overall, the two sites exhibit distinct coupling modes. Lanzhou features a "Pressure-Humidity-Trend" regime, where oxygen variability is controlled by the evolution of synoptic-scale pressure systems governing urban stability and dispersion. Conversely, Qomolangma follows a "Temperature-Pressure-Trend" regime. This is driven by the synergistic effects of thermal and dynamic processes, consistent with the thermally driven mountain-valley circulation and complex terrain transport characteristic of the region.

3.3. Interactions Between Atmospheric Oxygen and Air Pollutants

Black Carbon (BC) was selected as a proxy for regional combustion and emission activities (Chen et al., 2018), as it is the sole pollutant monitored concurrently at both stations. As a refractory carbonaceous aerosol formed exclusively during the incomplete combustion of carbon-based fuels, BC originates primarily from anthropogenic sources such as diesel transport, residential solid fuel combustion (Bond et al., 2013), and industrial operations. Crucially, a distinct mechanistic difference exists between these anthropogenic sources and natural biospheric processes: while combustion consumes O_2 and releases CO_2 accompanied by BC emissions, biological respiration and photosynthesis influence O_2 and CO_2 fluxes via enzymatic pathways without yielding elemental carbon (Manning & Keeling, 2006; Schlesinger & Bernhardt, 2020). This establishes a diagnostic framework where a strong BC-O_2 coupling indicates combustion dominance, whereas a decoupling suggests biospheric or background control.

To empirically test this relationship and mitigate noise from atmospheric turbulence and instrument variability, a Binning Trend Analysis was employed on the raw hourly data. The BC-ΔO_2 pairs were sorted by BC concentration and partitioned into 19 equidistant bins (excluding empty bins). For each bin, the mean ΔO_2 and its standard error were calculated and subjected to Ordinary Least Squares (OLS) linear regression to isolate systematic trends (Wilks, 2011). The regression results (Figures 4a and 4b) reveal a distinct contrast between the two sites. At Lanzhou station, located in a bustling urban hub with significant anthropogenic sources, ΔO_2 exhibits a strong near-linear decrease with increasing BC (Slope ≈ -14.6, $R^2 \approx 0.74$). This high correlation, combined with the steep negative slope, confirms that local anthropogenic combustion plays a pivotal role in regulating ΔO_2 variability at this urban site. Conversely, the Qomolangma station represents a remote, high-altitude environment with negligible local human interference. Here, the BC-ΔO_2 relationship (Slope ≈ 0.03, $R^2 \approx 0.18$) shows a near-zero slope, implying that BC accounts for only a minor fraction of ΔO_2 variations. This decoupling aligns with the

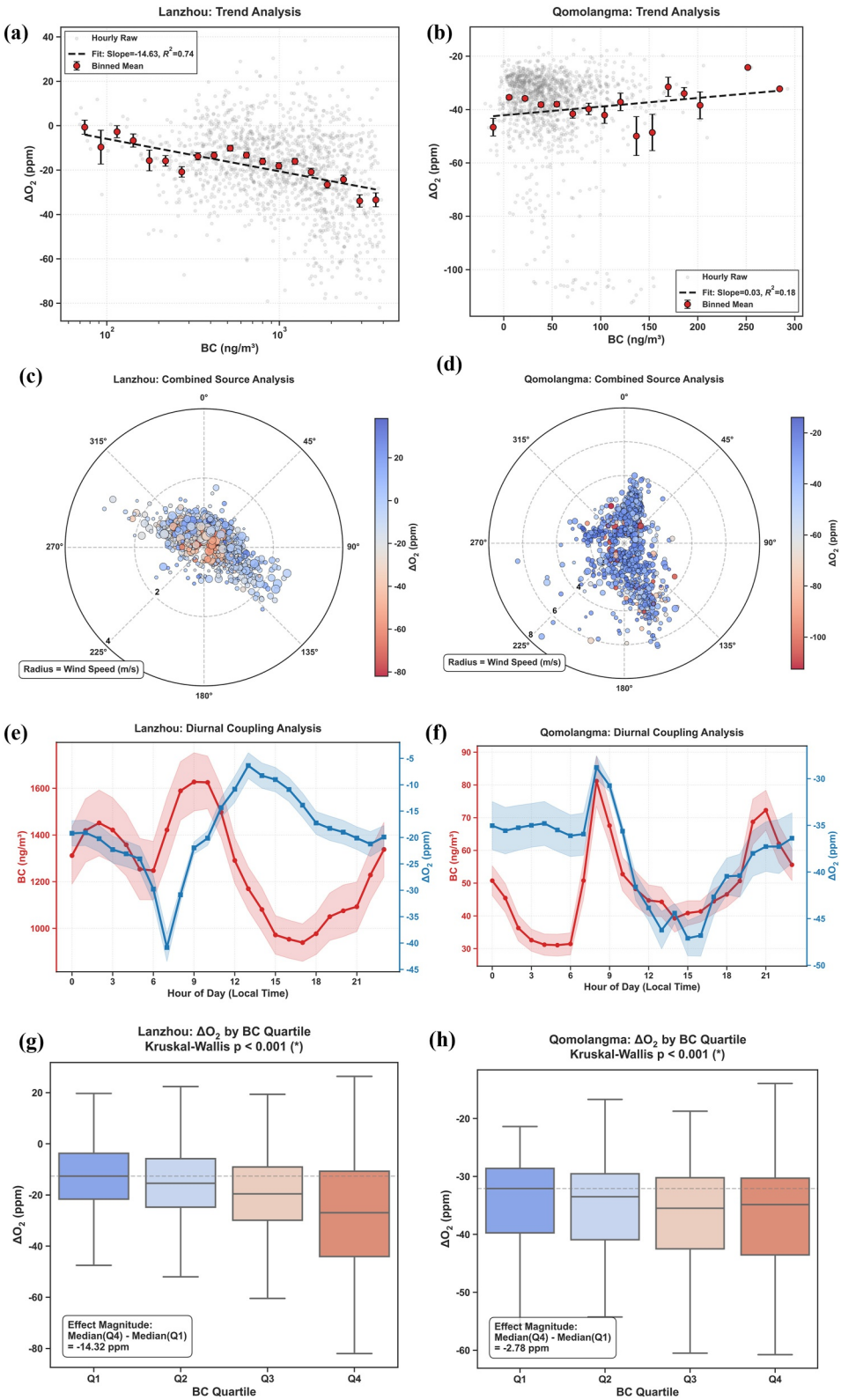

Figure 4. (a, b) Statistical relationships and trend analysis of BC and ΔO_2 at Lanzhou and Qomolangma sites. Panels (c, d) source attribution via bubble polar plots, Angle shows wind direction (0° = north, clockwise through east, south and west), radius is wind speed, bubble size is BC, and color is ΔO_2. Panels (e, f) spatiotemporal coupling characterized by dual-axis diurnal variations. Panels (g, h) statistical stratification of ΔO_2 across BC quartiles ((Q1 lowest–Q4 highest): boxes = IQR, thick line = median, diamond = mean, whiskers = 1.5 × IQR).

theoretical expectation for a remote site where natural biospheric processes and large-scale background transport modulate ΔO_2. The polar bubble plots (Figures 4c and 4d), which integrate wind and pollutant data, further clarify these dynamics. For Lanzhou, observations cluster predominantly within the low-wind regime (<2 m/s), where high BC levels and strong ΔO_2 fluctuations coincide. Spatially, the southeast-to-west sectors exhibit the most pronounced anomalies (visualized as large, red-hued bubbles), indicating that stagnant conditions facilitate the accumulation of local anthropogenic emissions, thereby driving oxygen decline. In contrast, higher wind speeds (>3 m/s) are associated with effective atmospheric dispersion, resulting in diluted pollutant concentrations and attenuated ΔO_2 fluctuations. Qomolangma, however, presents a distinctly different regime. The site is characterized by consistently low BC levels across all wind sectors, reflecting a clean background atmosphere. While sporadic elevated BC events occur within the weak-to-moderate wind range (1–4 m/s), their influence on ΔO_2 is limited and episodic. Under higher wind speeds (4–8 m/s), the dominance of baseline values suggests that the site is governed by free tropospheric background air, where ΔO_2 variability is driven by large-scale transport rather than local combustion sources.

Diurnal composites (Figures 4e and 4f) reveal a robust anti-correlation at Lanzhou, where ΔO_2 mirrors the characteristic bimodal BC profile. Significant oxygen depletion coincides with pollution peaks, recovering toward background levels in the afternoon. In contrast, Qomolangma exhibits no clear diurnal co-variation comparable to Lanzhou. BC-stratified boxplots (Figures 4g and 4h) quantify this disparity. Lanzhou exhibits a monotonic decline in median ΔO_2 from Q1 to Q4 with a substantial gap of 14.32 ppm. This significant gradient (Kruskal-Wallis test) reflects persistent depletion driven by local combustion emissions. Conversely, while statistically significant, the variation at Qomolangma is minimal (2.78 ppm).

To separate the BC-related contribution to ΔO_2 from dominant meteorological variability, we applied a PCA-GAM framework (Text S2), in which PC1 and PC2 summarize the leading meteorological states (Figure S11 in Supporting Information S1). Figure 5 shows the resulting two-dimensional partial-effect surfaces for ΔO_2. The left column presents the joint meteorological surface (PC1-PC2), whereas the middle and right columns show the PC1-BC and PC2-BC interaction surfaces, respectively. Warm and cool colors denote positive and negative partial contributions to ΔO_2, respectively, and closely spaced contours indicate steeper local gradients in the fitted surface. At Lanzhou, both interaction surfaces show clear gradients along the BC dimension, indicating that the ΔO_2 response to BC remains evident after accounting for meteorological variability. In particular, the PC2-BC surface suggests stronger BC sensitivity under lower-PC2 regimes, consistent with reduced ventilation inferred from the PCA loadings. In contrast, at Qomolangma, the interaction surfaces are less systematically aligned along the BC dimension, suggesting that ΔO_2 variability there is influenced more strongly by meteorological background variability than by a systematic BC effect.

3.4. Analysis of Oxygen Variability in the Urban Area

Building on the observed fluctuations in ΔO_2, we investigated the underlying photochemical and meteorological drivers from an interaction perspective (Figure 6). Our results reveal that urban oxygen variability is not a linear superposition of individual pollutants but a nonlinear process dominated by TVOCs and the NOx–O_3 cycle, intricately modulated by meteorological conditions, promoted by high temperatures and suppressed by strong winds and humidity.

To elucidate these dynamics, we analyzed aerosol and ozone episodes classified by vertically resolved measurements (Figures S12 and S13 in Supporting Information S1). Aerosol-polluted episodes were defined by lidar-derived extinction coefficients exceeding 0.5 km^{-1} at 532 nm (Yang et al., 2021), while ozone-polluted cases were characterized by maximum daily 8-hr average (MDA8) O_3 concentrations surpassing 160 $\mu g\ m^{-3}$, aligned with China's air quality standards (GB3095-2012).

The ventilation coefficient (VC), defined as the product of boundary layer height (BLH) and mean wind speed, is a key indicator of atmospheric dispersion capacity (Azargoshasbi et al., 2023). Higher VC values enhance pollutant dilution and reduce near-surface accumulation. While ΔO_2 generally exhibited a positive correlation with VC, confirming the foundational role of atmospheric dispersion, the sensitivity varied by pollution type. In aerosol-polluted scenarios, the dependence of ΔO_2 on local dispersion was relatively weak ($R = 0.38$) (Figure 7a). Despite boundary layer compression and strong inversions trapping pollutants (Figures S12 and S13 in Supporting Information S1), trajectory analysis (Figure 7c) identified a confounding factor: the longer-range northwesterly cluster (Cluster 2) showed weaker oxygen depletion (−12.9 ppm). The advection of less

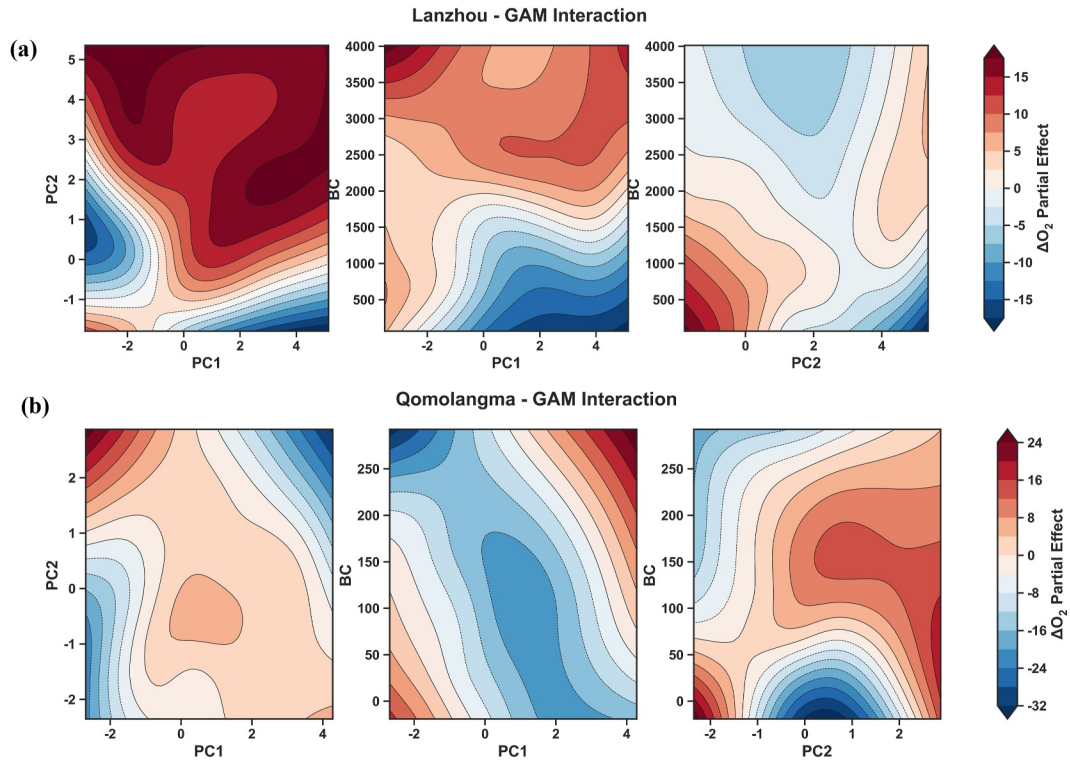

Figure 5. Two-dimensional partial-effect surfaces from the PCA-GAM models for ΔO_2 at (a) Lanzhou and (b) Qomolangma. In each row, the left column shows the joint meteorological surface (PC1-PC2), while the middle and right columns show the PC1-BC and PC2-BC interaction surfaces, respectively. Colors indicate partial contributions to ΔO_2, with warm and cool colors representing positive and negative effects.

oxygen-depleted air masses effectively offset local stagnation, thereby weakening the dependence of ΔO_2 on local ventilation constraints. Conversely, ozone-polluted scenarios exhibited high sensitivity to local meteorology ($R = 0.60$) (Figure 7b). Sensitivity analysis confirms that these correlation strengths are statistically robust and independent of sample size variations. Under low VC conditions (<2,000 $m^2\ s^{-1}$), ΔO_2 dropped sharply to $-30 \sim -40$ ppm. Long-range air masses originating from the northwest (Cluster 1) exhibited the most severe oxygen depletion (-23.3 ppm) (Figure 7d). This suggests a synergistic "external input–local amplification" mechanism for ozone-polluted scenario: long-range transport delivered abundant precursors and aged air masses, while the local high-temperature thermal structure (characterized by elevated potential temperature) further accelerated the precursor oxidation and photochemical ozone production. Crucially, the modulation of the oxygen budget is not limited to these concentration dynamics; it is further reshaped by the superposition of synoptic-scale pressure systems, as elucidated by the near-surface oxygen partial pressure (PiO_2, Figure S14 in Supporting Information S1). During aerosol episodes, a stagnant high-pressure ridge, characterized by sparse geopotential height contours and weak winds (Figure S14c in Supporting Information S1), dominated the synoptic pattern. This system induced subsidence and atmospheric compression, which mechanically elevated PiO_2 (Figure S14a in Supporting Information S1) and favored the accumulation of pollutants (Zhou et al., 2023). Conversely, ozone episodes were associated with low-pressure troughs and relatively higher humidity (Figure S14d in Supporting Information S1). This synoptic system intrinsically resulted in lower ambient pressure, leading to physically reduced PiO_2 levels (Figure S14b in Supporting Information S1). Unlike the stagnant conditions in aerosol cases, this convergent synoptic pattern likely facilitated the regional transport of precursors, while the presence of water vapor may have enhanced radical cycles, thereby sustaining conditions favorable for photochemical ozone production despite the lower pressure (Seinfeld & Pandis, 2016; Shu et al., 2016).

Having established that meteorological conditions and transport processes jointly shape ΔO_2 variability, a deeper investigation is required to identify the underlying chemical drivers. Specifically, from a chemical perspective, we aim to determine whether the observed ΔO_2 variability is dominated by primary combustion emissions or

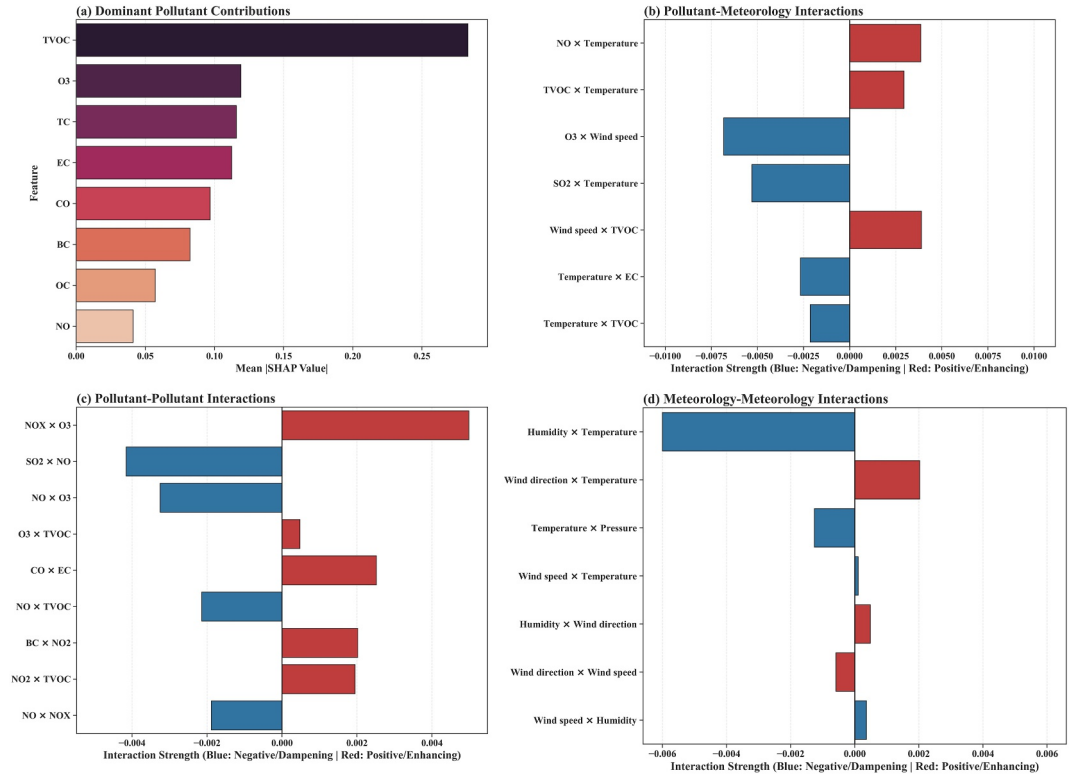

Figure 6. SHAP summary plots illustrating the drivers of ΔO_2 variations. Panel (a) global feature importance ranked by mean absolute SHAP values. Panels (b–d) interaction strengths for pollutant–meteorology, pollutant–pollutant, and meteorology–meteorology pairs. Red bars indicate positive (enhancing) interactions while blue bars indicate negative (dampening) interactions.

modulated by secondary photochemical transformations. To address this, carbon monoxide (CO) was selected as a reference tracer due to its source commonality with anthropogenic combustion, ecological inertness over short timescales, and its dual role as both a primary emission tracer and a secondary photochemical product (Parrish et al., 2011; Seinfeld & Pandis, 2016). Correlation analysis (Figure 7e) and the resulting oxidation ratios ($\Delta O_2/\Delta CO$) revealed a distinct shift in dominant oxygen-consuming processes (Figure 7f). During aerosol episodes, the observed slope was notably steep (~ -144.9). Consistent with the stable oxidative ratios (OR) of fossil fuels (1.17–1.44; Manning & Keeling, 2006), this value falls within the typical stoichiometric range for fossil fuel combustion ($\Delta O_2/\Delta CO \approx -OR \times \Delta CO_2/\Delta CO$) (Tohjima et al., 2014). A steeper $\Delta O_2/\Delta CO$ slope implies a larger $\Delta CO_2/\Delta CO$ ratio, indicative of higher average combustion efficiency (i.e., lower CO emission factors). This chemical fingerprint is consistent with the meteorological evidence for stagnation, suggesting that oxygen depletion during aerosol episodes was more strongly associated with the accumulation of primary combustion products than with secondary photochemical processing. Conversely, the slope flattened significantly (to -79.3) during ozone episodes. This shift is attributed to the secondary production of CO via VOC oxidation (Duncan et al., 2007; Kansal, 2009). Mechanistically, this process is driven by the moisture-enhanced radical cycles identified earlier, where high humidity accelerates hydroxyl radical (·OH) generation to catalyze the oxidation of hydrocarbons into secondary CO (Liang et al., 2019; Wu et al., 2020). This secondary source elevated ambient CO levels and consequently reduces the $\Delta O_2/\Delta CO$ ratio. This mechanism is corroborated by elevated i-Pentane/n-Pentane ratios observed during typical ozone events (Figure S15 in Supporting Information S1). The abundance of reactive light hydrocarbons from fuel evaporation provides ample precursors for secondary CO generation (Kumar et al., 2020; Wang et al., 2013), chemically validating the active photochemical environment hypothesis proposed in the previous section. Diurnal patterns (Figures 7g and 7h) further validate this divergence. While aerosol cases showed weaker correlation ΔO_2 and CO variations, likely attributed to the interference of non-combustion sources (e.g., dust), ozone cases exhibited a highly synchronized anti-phase relationship ($r = -0.61$), characterized by distinct negative coupling throughout the diurnal cycle. Multi-species analysis

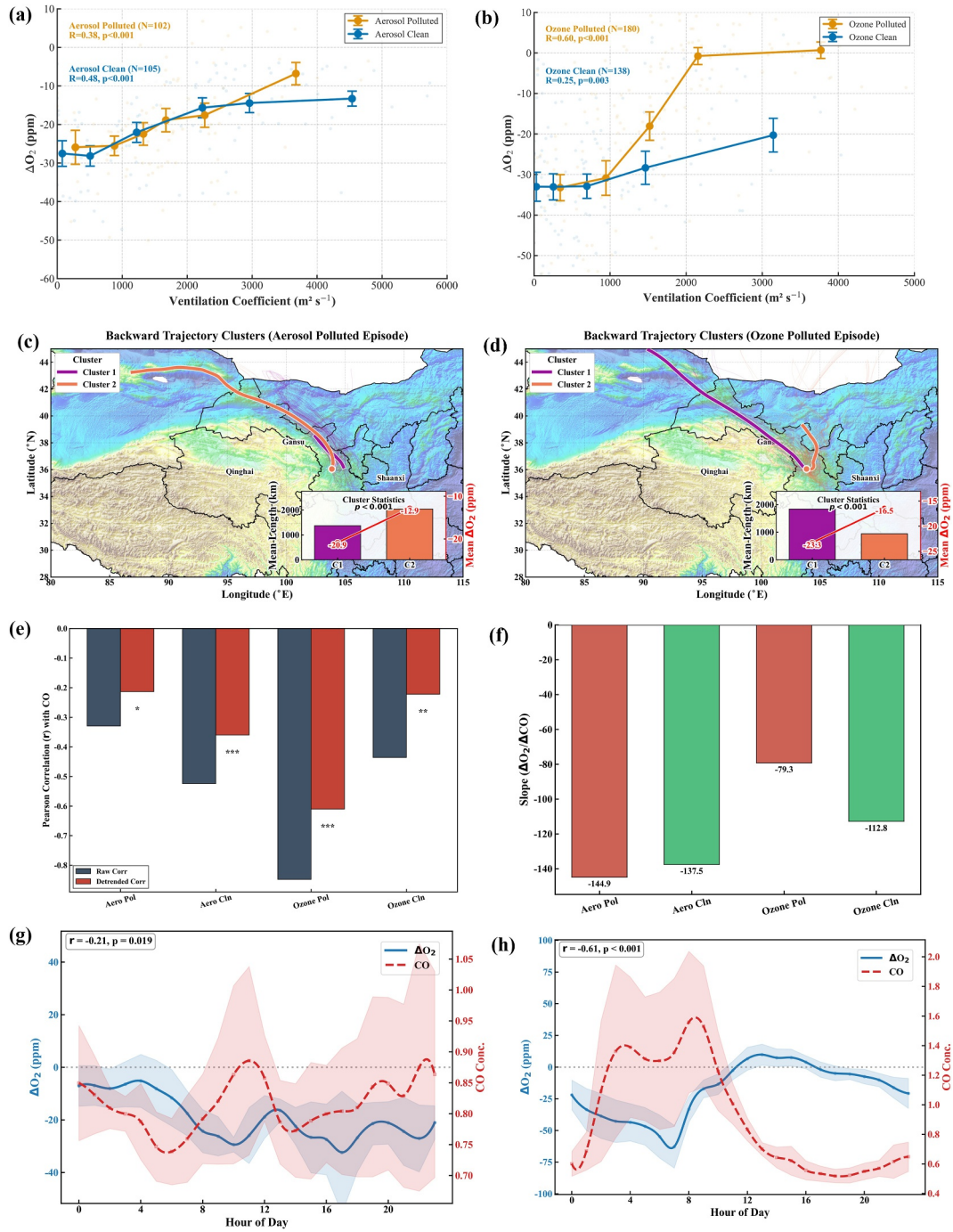

Figure 7. ΔO_2 versus ventilation coefficient (VC, $m^2\ s^{-1}$) for aerosol- (a) and ozone-dominated (b) episodes. Transport pathways identified by cluster analysis of backward trajectories for representative (c) aerosol and (d) ozone episodes. Thick curves denote cluster centroids; insets summarize statistics including mean trajectory length and associated ΔO_2. Panel (e) Pearson correlations between ΔO_2 and CO for raw (blue) versus meteorologically detrended (red) data across four scenarios (*$p < 0.05$). (f) Oxidation ratios ($\Delta O_2/\Delta CO$) derived from Orthogonal Distance Regression (ODR). Panels (g, h) comparison of detrended ΔO_2 residuals (solid blue, left axis) and CO concentrations (dashed red, right axis) for (g) aerosol-polluted and (h) ozone-polluted days. Shaded bands denote 95% confidence intervals. Abbreviations: Aero Pol (Aerosol Pollution), Aero Cln (Aerosol Clean), Ozone Pol (Ozone Pollution), and Ozone Cln (Ozone Clean).

(Figures S16 and S17 in Supporting Information S1) reinforces this finding: unlike the weak correlations observed in aerosol scenarios (likely due to external dust transport), ΔO_2 during ozone events showed strong synchronous variation with CO, BC, and O_3 ($p < 0.001$). Since BC is a strictly primary combustion product inert to secondary formation, its strong correlation confirms that the transported air masses comprised a co-mingled plume, integrating aged primary emissions with chemically evolved secondary pollutants (Bond et al., 2013; Petzold et al., 2013).

4. Conclusions

Deploying synchronized high-resolution observations for the first time at both an industrial urban valley (Lanzhou) and a remote high-altitude background site (Qomolangma Station), this study elucidates how urbanization perturbs the natural atmospheric O_2 cycle.

Our results identify a fundamental divergence in driving mechanisms: At the remote site, O_2 variability is dominated primarily by meteorological variability, especially thermodynamic coupling. In contrast, at the urban site, O_2 variability is strongly modulated by synoptic-scale pressure systems that regulate atmospheric stability and dispersion, while the anthropogenic ΔO_2-BC relationship remains robust after meteorological adjustment. Further analysis reveals a regime-dependent shift in the dominant controls on urban oxygen depletion. Aerosol episodes are characterized mainly by physical decoupling associated with stagnant accumulation and the advection of less oxygen-depleted air masses, whereas ozone episodes are characterized by chemical synergy arising from coupled external input and local photochemical amplification. In conclusion, our findings demonstrate that the urban oxygen cycle is not simply a passive response to emissions, but a dynamic system shaped by interactions among emissions, transport, and meteorology. This work provides a new perspective for understanding urban perturbations of atmospheric O_2 and for interpreting urban carbon-oxygen coupling under changing environmental conditions.

Conflict of Interest

The authors declare no conflicts of interest relevant to this study.

Availability Statement

Oxygen concentration data from the Lanzhou and Qomolangma stations were obtained through in situ continuous observations using Picarro G2207-i gas concentration and isotope analyzers operated by the Collaborative Innovation Center for West Ecological Safety (Collaborative Innovation Center for West Ecological Safety, 2025) (platform description available at: https://ciwes.lzu.edu.cn/yjfx/staqyyxh1/yjfxjj.htm). Pollutant and meteorological data sets were collected from online monitoring instruments managed by the Urban Climate and Environment Observatory of Lanzhou University (Urban Climate and Environment Observatory of Lanzhou University, 2022). Detailed information regarding the station's location and instrumentation is available at https://mcs.lzu.edu.cn/taizhanjianjie/2022/0520/196726.html. Model simulations were conducted using Python (version 3.10.9), packaged by Anaconda, Inc. (Anaconda, Inc., 2023).

Due to strict institutional data management policies protecting long-term station assets, these specific high-resolution observational data sets are not currently deposited in a public access repository. However, to facilitate scientific verification, the data and processing scripts are available for research purposes. Researchers may contact the corresponding author (hjp@lzu.edu.cn) to initiate the data request process, which requires a standard Data Use Agreement. This mechanism ensures transparency and compliance with the institutional data governance framework.

Acknowledgments
The work was supported by the National Natural Science Foundation of China (42595593), Natural Science Foundation of Gansu Province of China (24JRRA410), the Natural Science Foundation of Yunnan Province (202505AV340011), the "Lanzhou Special Fund for Talent Program", and the Fundamental Research Funds for the Central Universities (lzujbky-2025-jdzx01).

References

Anaconda, Inc. (2023). Anaconda distribution [Software]. Retrieved from https://www.anaconda.com

Azargoshasbi, F., Ashrafi, K., & Ehsani, A. H. (2023). Role of urban boundary layer dynamics and ventilation efficiency in a severe air pollution episode in Tehran, Iran. *Meteorology and Atmospheric Physics*, *135*(4), 35. https://doi.org/10.1007/s00703-023-00972-3

Bender, M. L., Battle, M., & Keeling, R. F. (1998). The O_2 balance of the atmosphere: A tool for studying the fate of fossil-fuel CO_2. *Annual Review of Energy and the Environment*, *23*(1), 207–223. https://doi.org/10.1146/annurev.energy.23.1.207

Bond, T. C., Doherty, S. J., Fahey, D. W., Forster, P. M., Berntsen, T., DeAngelo, B. J., et al. (2013). Bounding the role of black carbon in the climate system: A scientific assessment. *Journal of Geophysical Research: Atmospheres*, *118*(11), 5380–5552. https://doi.org/10.1002/jgrd.50171

Chen, X., Kang, S., Cong, Z., Yang, J., & Ma, Y. (2018). Concentration, temporal variation, and sources of black carbon in the Mt. Everest region retrieved by real-time observation and simulation. *Atmospheric Chemistry and Physics*, *18*(17), 12859–12875. https://doi.org/10.5194/acp-18-12859-2018

Cleveland, W. S. (1979). Robust locally weighted regression and smoothing scatterplots. *Journal of the American Statistical Association*, *74*(368), 829–836. https://doi.org/10.1080/01621459.1979.10481038

Collaborative Innovation Center for West Ecological Safety. (2025). *Research direction and platform introduction*. Lanzhou University. Retrieved from https://ciwes.lzu.edu.cn/yjfx/staqyyxh1/yjfxjj.htm

Denning, A. S., Randall, D. A., Collatz, G. J., & Sellers, P. J. (1996). Simulations of terrestrial carbon metabolism and atmospheric CO_2 in a general circulation model. Part 2: Simulated CO_2 concentrations. *Tellus B: Chemical and Physical Meteorology*, *48*(4), 543–567. https://doi.org/10.1034/j.1600-0889.1996.t01-1-00010.x

Duncan, B. N., Logan, J. A., Bey, I., Megretskaia, I. A., Yantosca, R. M., Novelli, P. C., et al. (2007). Global budget of CO, 1988–1997: Source estimates and validation with a global model. *Journal of Geophysical Research*, *112*(D22), 2007JD008459. https://doi.org/10.1029/2007JD008459

Fleming, L. S., Manning, A. C., Pickers, P. A., Forster, G. L., & Etchells, A. J. (2023). Evaluating the performance of a Picarro G2207-i analyser for high-precision atmospheric O_2 measurements. *Atmospheric Measurement Techniques*, *16*(2), 387–401. https://doi.org/10.5194/amt-16-387-2023

Ginzburg, A. S., Vinogradova, A. A., Lezina, E. A., & Pomelova, M. A. (2023). Changes in the oxygen content in urban air under the influence of natural and anthropogenic factors. *Izvestiya Atmospheric and Oceanic Physics*, *59*(4), 378–389. https://doi.org/10.1134/S0001433823040060

Hoerl, A. E., & Kennard, R. W. (1970). Ridge regression: Biased estimation for nonorthogonal problems. *Technometrics*, *12*(1), 55–67. https://doi.org/10.1080/00401706.1970.10488634

Hu, X., Chen, Y., Huo, W., Jia, W., Ma, H., Ma, W., et al. (2023). Surface oxygen concentration on the Qinghai-Tibet Plateau (2017–2022). *Scientific Data*, *10*(1), 900. https://doi.org/10.1038/s41597-023-02768-x

Huang, J., Huang, J., Liu, X., Li, C., Ding, L., & Yu, H. (2018). The global oxygen budget and its future projection. *Science Bulletin*, *63*(18), 1180–1186. https://doi.org/10.1016/j.scib.2018.07.023

Huang, J., Liu, X., He, Y., Shen, S., Hou, Z., Li, S., et al. (2021). The oxygen cycle and a habitable Earth. *Science China Earth Sciences*, *64*(4), 511–528. https://doi.org/10.1007/s11430-020-9747-1

Kansal, A. (2009). Sources and reactivity of NMHCs and VOCs in the atmosphere: A review. *Journal of Hazardous Materials*, *166*(1), 17–26. https://doi.org/10.1016/j.jhazmat.2008.11.048

Keeling, R. F., & Manning, A. C. (2014). Studies of recent changes in atmospheric O_2 content. In *Treatise on geochemistry* (2nd ed., Vol. 5, pp. 385–404). https://doi.org/10.1016/B978-0-08-095975-7.00420-4

Keeling, R. F., Najjar, R. P., Bender, M. L., & Tans, P. P. (1993). What atmospheric oxygen measurements can tell us about the global carbon cycle. *Global Biogeochemical Cycles*, *7*(1), 37–67. https://doi.org/10.1029/92GB02733

Keeling, R. F., Piper, S. C., & Heimann, M. (1996). Global and hemispheric CO_2 sinks deduced from changes in atmospheric O_2 concentration. *Nature*, *381*(6579), 218–221. https://doi.org/10.1038/381218a0

Kumar, A., Sinha, V., Shabin, M., Hakkim, H., Bonsang, B., & Gros, V. (2020). Non-methane hydrocarbon (NMHC) fingerprints of major urban and agricultural emission sources for use in source apportionment studies. *Atmospheric Chemistry and Physics*, *20*(20), 12133–12152. https://doi.org/10.5194/acp-20-12133-2020

Larson, V. E., & Volkmer, J. (2008). An idealized model of the one-dimensional carbon dioxide rectifier effect. *Tellus B: Chemical and Physical Meteorology*, *60*(3), 287–297. https://doi.org/10.1111/j.1600-0889.2008.00368.x

Liang, L., Engling, G., Cheng, Y., Zhang, X., Sun, J., Xu, W., et al. (2019). Influence of high relative humidity on secondary organic carbon: Observations at a background site in East China. *Journal of Meteorological Research*, *33*(5), 905–913. https://doi.org/10.1007/s13351-019-8202-2

Liu, X., Huang, J., Wang, L., Lian, X., Li, C., Ding, L., et al. (2023). Urban respiration" revealed by atmospheric O_2 measurements in an industrial metropolis. *Environmental Science & Technology*, *57*(6), 2286–2296. https://doi.org/10.1021/acs.est.2c07583

Manning, A., & Keeling, R. F. (2006). Global oceanic and land biotic carbon sinks from the Scripps atmospheric oxygen flask sampling network. *Tellus B: Chemical and Physical Meteorology*, *58*(2), 95–116. https://doi.org/10.1111/j.1600-0889.2006.00175.x

Manning, A. C., Keeling, R. F., & Severinghaus, J. P. (1999). Precise atmospheric oxygen measurements with a paramagnetic oxygen analyzer. *Global Biogeochemical Cycles*, *13*(4), 1107–1115. https://doi.org/10.1029/1999gb900054

Morgan, E. J., Stephens, B. B., Long, M. C., Keeling, R. F., Bent, J. D., McKain, K., et al. (2019). Summertime atmospheric boundary layer gradients of O_2 and CO_2 over the Southern Ocean. *Journal of Geophysical Research: Atmospheres*, *124*(23), 13439–13456. https://doi.org/10.1029/2019JD031479

Padarian, J., McBratney, A. B., & Minasny, B. (2020). Game theory interpretation of digital soil mapping convolutional neural networks. *SOIL*, *6*(2), 389–397. https://doi.org/10.5194/soil-6-389-2020

Parrish, D. D., Singh, H. B., Molina, L., & Madronich, S. (2011). Air quality progress in North American megacities: A review. *Atmospheric Environment*, *45*(39), 7015–7025. https://doi.org/10.1016/j.atmosenv.2011.09.039

Petzold, A., Ogren, J. A., Fiebig, M., Laj, P., Li, S.-M., Baltensperger, U., et al. (2013). Recommendations for reporting "black carbon" measurements. *Atmospheric Chemistry and Physics*, *13*(16), 8365–8379. https://doi.org/10.5194/acp-13-8365-2013

Pickers, P. A., Manning, A. C., Le Quéré, C., Forster, G. L., Luijkx, I. T., Gerbig, C., et al. (2022). Novel quantification of regional fossil fuel CO_2 reductions during COVID-19 lockdowns using atmospheric oxygen measurements. *Science Advances*, *8*(16), eabl9250. https://doi.org/10.1126/sciadv.abl9250

Schlesinger, W. H., & Bernhardt, E. S. (2020). *Biogeochemistry: An analysis of global change* (4th ed.). Academic Press.

Seinfeld, J. H., & Pandis, S. N. (2016). *Atmospheric chemistry and physics: From air pollution to climate change*. John Wiley & Sons.

Shi, P., Chen, Y., Zhang, G., Tang, H., Chen, Z., Yu, D., et al. (2021). Factors contributing to spatial–temporal variations of observed oxygen concentration over the Qinghai-Tibetan Plateau. *Scientific Reports*, *11*(1), 17338. https://doi.org/10.1038/s41598-021-96741-6

Shu, L., Xie, M., Wang, T., Gao, D., Chen, P., Han, Y., et al. (2016). Integrated studies of a regional ozone pollution synthetically affected by subtropical high and typhoon system in the Yangtze River Delta region, China. *Atmospheric Chemistry and Physics*, *16*(24), 15801–15819. https://doi.org/10.5194/acp-16-15801-2016

Sun, F., Ma, Y., Hu, Z., Li, M., Tartari, G., Salerno, F., et al. (2018). Mechanism of daytime strong winds on the northern slopes of Himalayas, near Mount Everest: Observation and simulation. *Journal of Applied Meteorology and Climatology*, *57*(2), 255–272. https://doi.org/10.1175/JAMC-D-16-0409.1

Tohjima, Y. (2000). Method for measuring changes in the atmospheric O_2/N_2 ratio by a gas chromatograph equipped with a thermal conductivity detector. *Journal of Geophysical Research*, *105*(D11), 14575–14584. https://doi.org/10.1029/2000jd900057

Tohjima, Y., Kubo, M., Minejima, C., Mukai, H., Tanimoto, H., Ganshin, A., et al. (2014). Temporal changes in the emissions of CH_4 and CO from China estimated from CH_4/CO_2 and CO/CO_2 correlations observed at Hateruma Island. *Atmospheric Chemistry and Physics*, *14*(3), 1663–1677. https://doi.org/10.5194/acp-14-1663-2014

Urban Climate and Environment Observatory of Lanzhou University. (2022). *Introduction to the urban climate and environment observatory platform, college of atmospheric sciences*. Lanzhou University. Retrieved from https://mcs.lzu.edu.cn/taizhanjianjie/2022/0520/196726.html

Wang, M., Shao, M., Lu, S.-H., Yang, Y.-D., & Chen, W.-T. (2013). Evidence of coal combustion contribution to ambient VOCs during winter in Beijing. *Chinese Chemical Letters*, *24*(9), 829–832. https://doi.org/10.1016/j.cclet.2013.05.029

Wei, Y., Wu, J., Huang, J., Liu, X., Han, D., An, L., et al. (2021). Declining oxygen level as an emerging concern to global cities. *Environmental Science & Technology*, *55*(12), 7808–7817. https://doi.org/10.1021/acs.est.1c00553

Wilks, D. S. (2011). *Statistical methods in the atmospheric sciences*. Academic Press.

Willmott, C. J. (1981). On the validation of models. *Physical Geography*, *2*(2), 184–194. https://doi.org/10.1080/02723646.1981.10642213

Wu, C., Wang, C., Wang, S., Wang, W., Yuan, B., Qi, J., et al. (2020). Measurement report: Important contributions of oxygenated compounds to emissions and chemistry of volatile organic compounds in urban air. *Atmospheric Chemistry and Physics*, *20*(23), 14769–14785. https://doi.org/10.5194/acp-20-14769-2020

Yang, H., Fang, Z., Xie, C., Cohen, J., Yang, Y., Wang, B., et al. (2021). Two trans-boundary aerosol transport episodes in the western Yangtze River Delta, China: A perspective from ground-based LiDAR observation. *Atmospheric Pollution Research*, *12*(3), 370–380. https://doi.org/10.1016/j.apr.2021.01.004

Zhou, X., Gao, X., Chang, Y., Zhao, S., & Li, P. (2023). The pattern and mechanism of an unhealthy air pollution event in Lanzhou, China. *Urban Climate*, *48*, 101409. https://doi.org/10.1016/j.uclim.2023.101409